ACSNANO

www.acsnano.org

ARTICLE

Chirally Selective and Switchable Luminescence from Achiral Quantum Emitters on Suspended Twisted Stacking Metasurfaces

Mengjia Cen,[#] Jianxun Liu,[#] Jiawei Wang, Ye Li, Wenfeng Cai, Ming Cheng, Delai Kong, Xiaoying Tang, Tun Cao,* Yan-Qing Lu,* and Yan Jun Liu*

Cite This: *ACS Nano* 2024, 18, 20556−20566

Read Online

ACCESS | Metrics & More | Article Recommendations | Supporting Information

ABSTRACT: **Dynamic control of circularly polarized photoluminescence has aroused great interest in quantum optics and nanophotonics. Chiral plasmonic metasurfaces enable the manipulation of the polarization state via plasmon-photon coupling. However, current plasmonic light-emitting metasurfaces for effective deterministic modulation of spin-dependent emission at near-infrared wavelengths are underexplored in terms of dissymmetry and tunability. Here, we demonstrate a microfluidic hybrid emitting system of a suspended twisted stacking metasurface coated with PbS quantum dots. The suspended metasurface is fabricated with a single step of electron beam exposure, exhibiting a strong optical chirality of 309° μm^{-1} with a thickness of less than $\lambda/10$ at key spectral locations. With significant chiral-selective interactions, enhanced photoluminescence is achieved with strong dissymmetry in circular polarization. The dissymmetry factor of the induced circularly polarized emission can reach 1.54. More importantly, altering the refractive index of the surrounding medium at the bottom surface of the metasurface can effectively manipulate the chiroptical responses of the hybrid system, hence leading to chirality-reversed emission. This active hybrid emitting system could be a resultful platform for chirality-switchable light emission from achiral quantum emitters, holding great potential for anticounterfeiting, biosensing, light sources, imaging, and displays.**

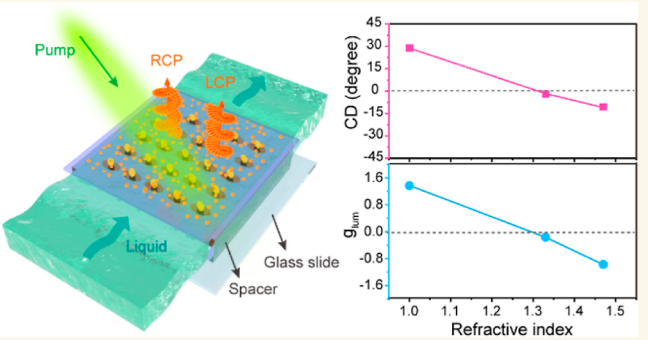

KEYWORDS: *active metasurface, optical chirality, circularly polarized luminescence, dissymmetry factor, plasmonic enhancement*

Downloaded via NANJING UNIV on May 10, 2025 at 13:17:44 (UTC).
See https://pubs.acs.org/sharingguidelines for options on how to legitimately share published articles.

INTRODUCTION

Chiral nanomaterials with strong and switchable chiroptical performance, such as circular dichroism (CD) and circularly polarized luminescence (CPL), have been thoroughly studied because of their potential applications in the realm of chiral photonics,[1−3] information encryption and storage,[4,5] asymmetric catalysis,[6] biosensing,[7,8] and three-dimensional displays.[9] Thus far, intensive efforts have been devoted to exploring artificial CPL-active materials in organic and inorganic systems.[10−12] Most organic CPL-active materials can be obtained by uniting the chiral moieties and emitters via covalent bonds. However, the synthesis procedure is complicated, and the luminescence dissymmetry factor (g_{lum}) for qualifying the degree of CPL remains very low (10^{-5} to 10^{-3}) owing to the negligible magnetic dipole transition moment.[13,14] Besides, chirality induction and transfer can be performed in inorganic materials via ligand-induced chirality and chiral self-assembly nanostructures.[15−17] Although the g_{lum} values can generally be amplified by one or 2 orders of magnitude, these inorganic systems still exhibit relatively weak chiroptical performance, which greatly limits their practical application scenarios.[18,19] Therefore, it is highly demanded to develop efficient approaches to constructing CPL-active materials with high and tunable chiroptical performance for various CPL-based applications.

Chiral metasurfaces, lacking inversion and mirror symmetry in subwavelength meta-atoms, have drawn tremendous attention for their aptitudes for modulating chiroptical responses and boosting optical activities.[20−22] Moreover, the

Received: April 29, 2024
Revised: July 1, 2024
Accepted: July 5, 2024
Published: July 15, 2024

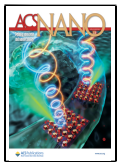

ACS Publications

© 2024 American Chemical Society

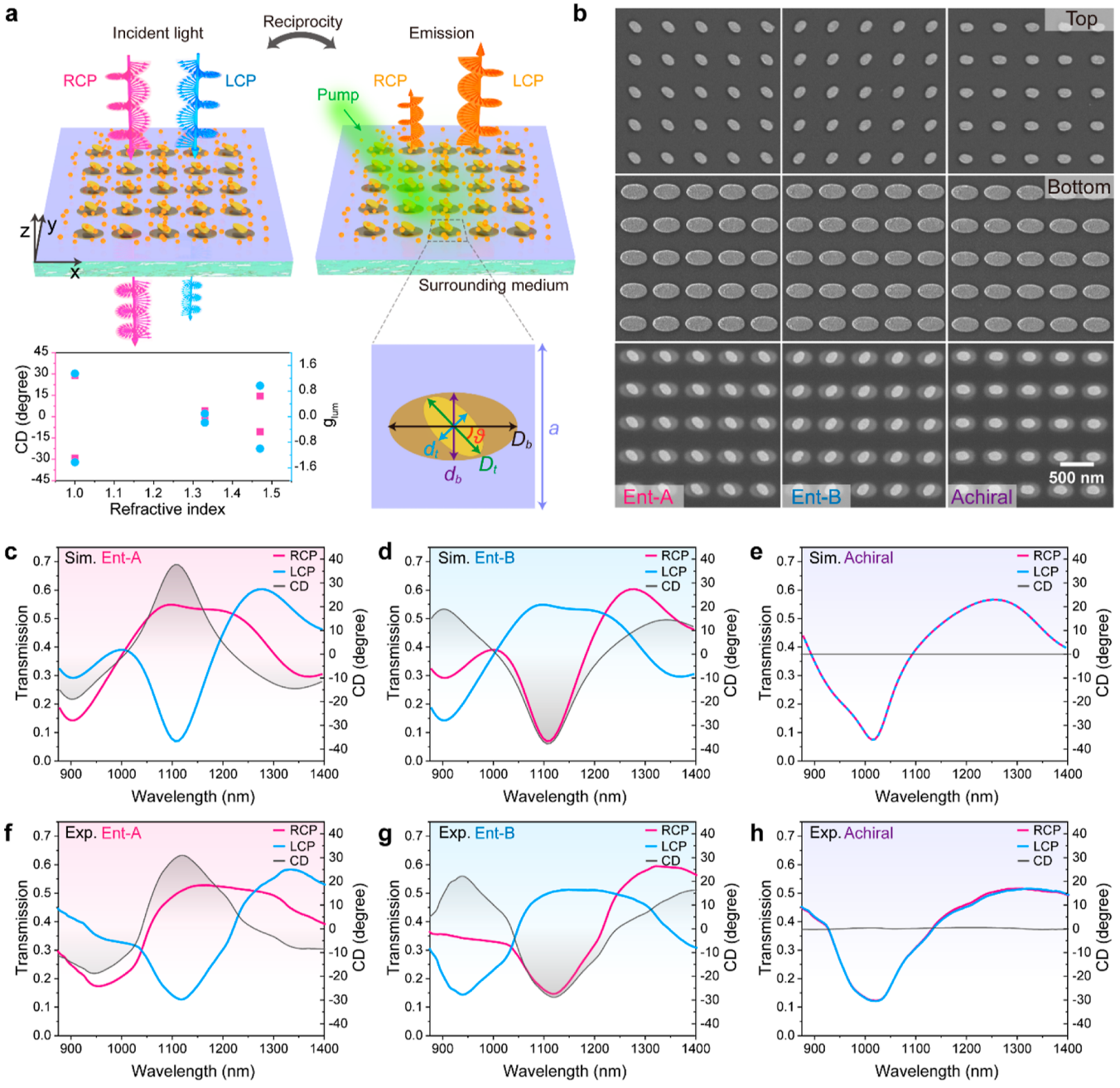

Figure 1. Design of the suspended twisted stacking metasurface. (a) Schematic diagram for the reciprocity of switchable chiral emission on the suspended metasurface. (b) SEM images of the top and bottom surfaces of enantiomer A, enantiomer B, and the achiral metasurface. Scale bar: 500 nm. (c–e) Simulated transmission spectra of enantiomer A (c), enantiomer B (d), and achiral metasurfaces (e) under RCP (magenta curve) and LCP (blue curve) incidence, respectively. (f–h) Experimentally measured transmission spectra of enantiomer A (f), enantiomer B (g), and achiral metasurfaces (h) under RCP (magenta curve) and LCP (blue curve) incidence, respectively.

planarization of metasurfaces[23] is conducive to realizing compact optical devices and reducing optical loss, which makes the chiral metasurfaces an applicable platform for constructing high-efficiency CPL-active systems. To date, polarization-dependent light-matter interactions in chiral metasurfaces have been increasingly exploited to enhance the intensity of photoluminescence (PL) and modulate the CPL from achiral organic and inorganic light emitters, such as dye molecules,[24,25] perovskite nanocrystals,[26,27] upconversion nanoparticles,[28] and semiconductor quantum dots (QDs).[29−31] The integration of emitters and metasurfaces enables attractive functional emission; however, compared to tunable self-assembled CPL-active materials,[32] most of the current emitter-metasurface composites suffer from rigid substrates, undeformable nanostructures, unchangeable surrounding mediums, and fixed emitter films, posing great hurdles for tuning chiral emission. Although various reconfigurable metasurfaces have been employed for dynamic optics via external stimuli,[33−36] their integration with emitters still remains a grand challenge. Only several metasurface systems have been demonstrated with dynamic tuning of the intensity and spectrum of spontaneous emission. One scheme for tuning the emission is electrical modulation by applying an external bias voltage.[37] Another notable strategy is to change the

https://doi.org/10.1021/acsnano.4c05719
ACS Nano 2024, 18, 20556−20566

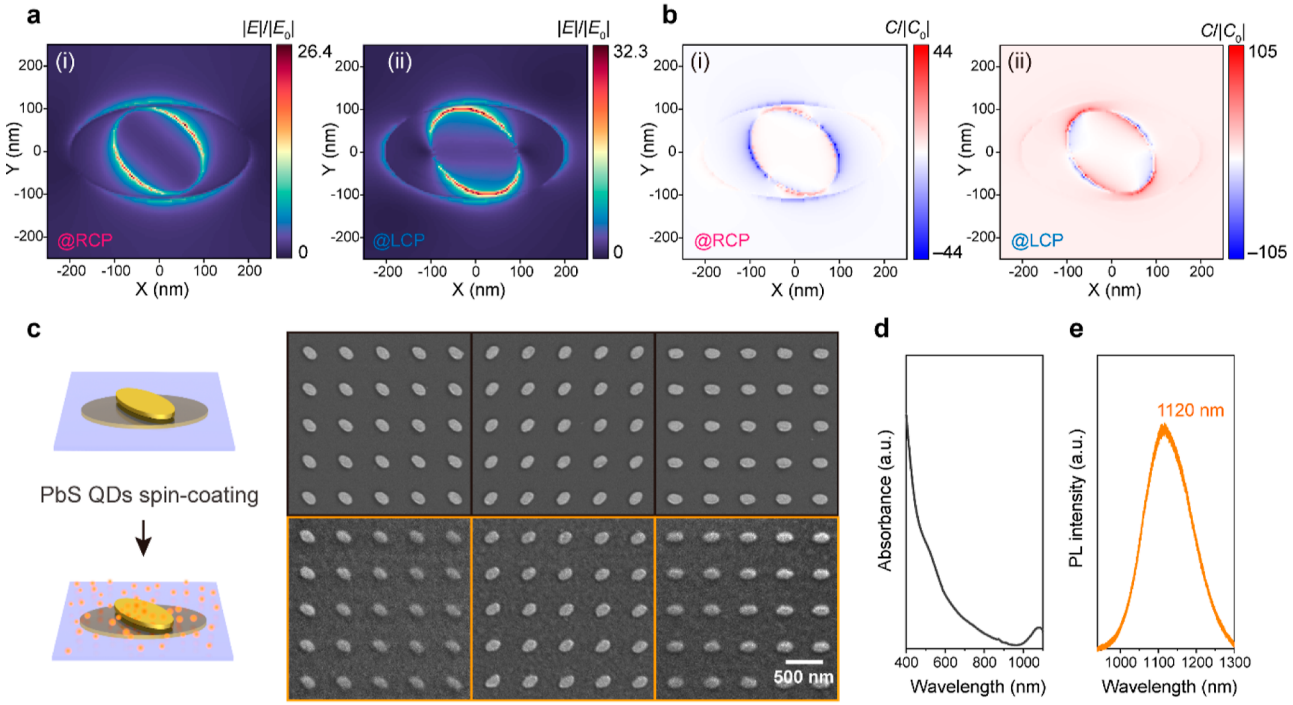

Figure 2. Design of the hybrid emitter-metasurface system. (a) Simulated distributions of electric field enhancements in enantiomer A under RCP (i) and LCP (ii) light at the extrema of the CD spectrum located at 1110 nm. (b) Simulated distributions of superchiral fields in enantiomer A under RCP (i) and LCP (ii) light at 1110 nm. (c) Schematic illustration of spin-coating PbS QDs on the top side of the metasurface. SEM images of the bottom surfaces for bare metasurfaces (black frame) and metasurfaces coated with PbS QDs (orange frame). Scale bar: 500 nm. (d) Absorbance spectrum of the PbS QDs solution. (e) PL spectrum of the PbS QDs spin-coated on a blank Si substrate.

refractive index of surrounding mediums.[38,39] Humidity-driven QD-containing hydrogel provides tunability for far-field emission modulation as well.[40] Nevertheless, tunable manipulation of the polarization of chiral emission based on chiral metasurfaces has not yet been extensively explored, much less polarity switching.

In this work, we propose an active hybrid emitting system based on suspended metasurfaces for modulating the chiral emission from the achiral PbS QDs. The suspended metasurface is fabricated by single-step electron beam lithography (EBL), consisting of two layers of twisted stacking gold nanoarrays spaced by a Si_3N_4 membrane. A strong chiroptical response with an optical chirality of 309° μm^{-1} is achieved in the near-infrared region. By spin-coating PbS QDs on this chiral metasurface, the hybrid emitting system manifests strong enhancement and preferential spin state modulation of CPL. The maximum value of g_{lum} can reach 1.54 at an emission wavelength of 1120 nm. More importantly, switchable chiral luminescence with inverse g_{lum} signs is achieved by controlling the chiroptical responses of the microfluidic hybrid emitting system via alteration of the surrounding medium at the bottom surface of the metasurface. The g_{lum} at the emission wavelength is tuned from −1.42 to 0.98, with a significant difference of 2.4. With the intention of unequivocally revealing the coupling mechanism between the QDs and plasmonic metasurfaces, we investigate the chiral properties of both transmission and emission processes via the reciprocity principle. We show that the achiral QDs are chiral-dependently functionalized by the plasmon-photon coupling on the metasurface, and the g_{lum} of the induced CPL is associated with the CD of the hybrid emitting system. The results provide a viable route to dynamically control the polarization properties of CPL with chiroptical tuning response.

RESULTS AND DISCUSSION

Suspended Twisted Stacking Metasurfaces. At the chiral plasmonic resonance region, distinct field enhancements can be generated for the right and left circularly polarized (RCP and LCP) light incidence, resulting in different chiral emissions according to the reciprocity theorem. The reciprocity principle implies that the CPL from the hybrid emitting system can be effectively controlled by modulating the chiral resonances. Thus far, most reported light-emitting metasurfaces do not possess the capability of actively tuning the polarization of luminescence. Our work shows that the suspended twisted stacking metasurface with double-sided exposed structures can be employed as a platform to generate switchable chiral emission. The geometry of the metasurface is depicted in the Figure 1a. The meta-atom is composed of two twisted, stacking gold elliptic cylinders spaced by a Si_3N_4 membrane. Emitters are spin-coated on the top surface, and the switchable surrounding medium is in contact with the bottom surface. The Si_3N_4 membrane serves as not only a supporting layer for meta-atoms but also an isolating barrier between emitters and an active surrounding medium for keeping the emitters stable. By changing the surrounding medium with different refractive indices, the CD and g_{lum} factors at the emission wavelength of the hybrid emitting system can be effectively tuned.

In this work, we investigate arrays of both chiral and achiral meta-atoms supported by Si_3N_4 membranes. The process flow of fabrication is shown in Figure S1. We emphasize that the top and bottom nanostructures are perfectly self-aligned with a

https://doi.org/10.1021/acsnano.4c05719
ACS Nano 2024, 18, 20556−20566

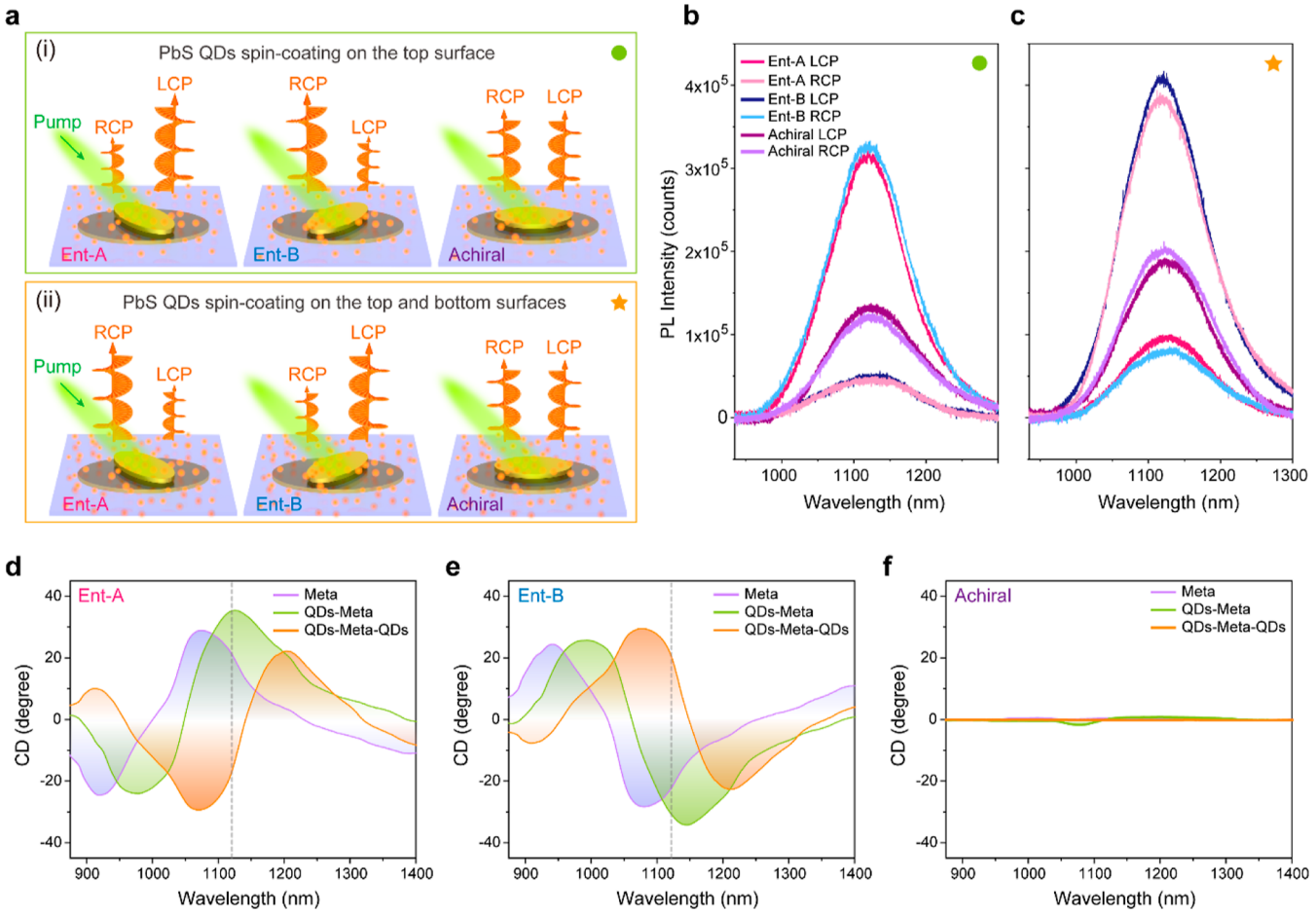

Figure 3. CPL and CD measured from a hybrid emitter-metasurface system. (a) Schematic illumination of PL investigation from QDs-metasurface and QDs-metasurface-QDs composites. Top: Three types of metasurfaces with PbS QDs spin-coated on the top surface for the comparative measurements. Bottom: Three types of metasurfaces with QDs spin-coated on both top and bottom surfaces. (b) RCP and LCP PL intensity from the metasurfaces with a single QD layer on the top surface. (c) RCP and LCP PL intensity from the metasurfaces with QDs layers on both top and bottom surfaces. (d–f) CD spectra of the hybrid systems for enantiomer A (d), enantiomer B (e), and achiral (f) metasurfaces, respectively. The dashed gray line represents the emission wavelength.

single-step EBL process, hence dispensing with the misalignment. The optimized structural parameters of the metasurfaces are D_t = 220 nm, d_t = 160 nm, D_b = 400 nm, d_b = 220 nm, a = 500 nm. The thicknesses of the Si_3N_4 membrane, top, and bottom Au layers are 50, 25, and 25 nm, respectively. ϑ gives the angle between the two major axes of the elliptic cylinders. Altering the twisted angle ϑ enabled strong chiroptical responses. CD is generated from the difference between the transmission spectra of two circular polarizations, and it can be calculated as the ellipticity angle given by the following equation[41,42]

$$\mathrm{CD} = \tan^{-1}\frac{T_{\mathrm{RCP}} - T_{\mathrm{LCP}}}{T_{\mathrm{RCP}} + T_{\mathrm{LCP}}} \quad (1)$$

where T_{RCP} and T_{LCP} indicate the transmission under RCP and LCP light, respectively. When ϑ is ±45°, the CD of the chiral metasurface reaches its maximum, as shown in Figure S2. The scanning electron microscopy (SEM) images of the chiral and achiral metasurfaces are shown in Figure 1b. For the enantiomer A, enantiomer B, and achiral metasurface, ϑ is −45°, 45°, and 0°, respectively.

Twisted stacking metasurfaces can selectively transmit light with specific handedness due to the near-field plasmonic coupling between the top and bottom nanostructures. The designed chirality-related resonant dip of enantiomer A and enantiomer B, which can be seen in Figure 1c,d, occurs at roughly 1110 nm. At the wavelength of the chiral resonance in the simulations, the CD reaches as large as 37.7°. As expected, Figure 1e illustrates that the transmission spectra of the achiral metasurface have no circular polarization dependency under RCP and LCP light. The experimentally measured transmission spectra shown in Figure 1f–h match well with the numerical calculations. The slight dissimilarity between the simulated and experimental spectra could be mainly attributed to imperfect fabrication and morphological variances in detailed features in the model. In addition, we simulated and measured the transmission spectra of various input–output handedness combinations (Figure S3). As can be seen, the strong CD is mainly produced by the disparity of the transmission for copolarized light since the transmitted light of cross-polarization is almost negligible. For enantiomer A, the measured CD value reaches 30.9° around 1120 nm. The enantiomer B shows a nearly opposite CD of −28.8° at the wavelength of 1120 nm. With the total thickness of 100 nm of the bilayer metasurface, the measured optical chirality is up to 309° μm^{-1}, which is significantly greater than the maximal value among the reported works of chiral metasurfaces (see

https://doi.org/10.1021/acsnano.4c05719
ACS Nano 2024, 18, 20556–20566

Table S1 and Figure S4 for details.).[43−46] The high optical chirality of twisted stacking metasurfaces supports strong chiral light−matter interactions in the near field, which is promising to enhance chiral emission.

Chiral-Selective Enhancement of Photoluminescence via Integration of Emitters and Metasurfaces. To reveal the underlying mechanisms of the chiroptical responses in the metasurfaces, we performed full-wave electromagnetic simulations to calculate the near-field features. Figures 2a,b and S5 show the simulated distributions of electric field enhancements and superchiral fields on the top and bottom interfaces in between the Si_3N_4 membrane and Au elliptic cylinders at the same time. Our suspended bilayer metasurface with the exposed top and bottom nanostructures is in vast contrast with other bilayer designs usually supported by substrates, which further facilitates strong chiral light−matter interactions on both the top and bottom surfaces. The intense electric fields are located at the interfaces between the Si_3N_4 membrane and the gold elliptic cylinders at the CD peak of 1110 nm. For enantiomer A, the enhancement factor of the electric field under LCP light is up to 32.3, which is higher than the enhancement factor of 26.4 under RCP illumination. The higher enhancement provides more resonance-based light confinement, which explains the higher absorption in Figure S6. Moreover, the enhanced field induced by circularly polarized light implies stronger emission of opposite helicity via reciprocity. Furthermore, we calculated the superchiral field $\boldsymbol{C}$ to quantify the near-field chirality for investigating its interaction with matter. The superchiral field distributions are determined by the presence of parallel components for the electric and magnetic fields[47,48]

$$\boldsymbol{C} = -\frac{\varepsilon_0 \omega}{2}\mathrm{Im}[\boldsymbol{E}^* \times \boldsymbol{B}] \tag{2}$$

where ε_0 is the permittivity of vacuum, ω is the angular frequency, and $\boldsymbol{E}$ and $\boldsymbol{B}$ are the local electric and magnetic fields, respectively. The local enhancement of the superchiral field is derived as $\boldsymbol{C}/|\boldsymbol{C}_0|$, and $\boldsymbol{C}_0$ is the value obtained without the metasurfaces. The sign $\boldsymbol{C}$ represents the different handedness of the local field. The positive sign indicates LCP, while the negative sign denotes RCP. The enhancements of the superchiral fields with LCP and RCP light at 1110 nm exhibit strong dependence on the spin state of the incident light. Figure 2a,b clearly shows distinct intensities on the top and bottom sides of the suspended metasurfaces, in which the top surface has stronger local fields.

Therefore, for obtaining intense chiral-selective emission, we introduce a hybrid emitting system in which the top side of metasurfaces is coated with achiral PbS QDs, as illustrated in Figure 2c. The SEM images in Figure 2c show the plasmonic metasurfaces before and after spin-coating PbS QDs. We measured the element composition and distribution of the PbS QDs on the metasurface (Figure S7) to confirm the homogeneous distribution of the QDs. In Figure 2d,e, we show the typical absorbance and PL spectra of PbS QDs, respectively. As evident from the absorbance spectrum, excitation at higher energies is favorable for the PL measurements. Thus, the top side of the metasurface was illuminated with an excitation laser at 532 nm, and the PL of QDs was collected from the top side. A 550 nm long-pass filter was set in the light path to prevent light from passing through the pump laser. The PL spectrum has an emission peak near 1120 nm, which almost overlays the characteristic CD peak of the chiral plasmonic metasurfaces.

As illustrated in Figure 3a, in order to ensure that measured differences are indeed structural effects, both chiral and achiral arrays were investigated. Notably, since the CD peak will be red-shifted when the metasurfaces are spin-coated with QDs due to the decreased refractive index contrast between the Si_3N_4 membrane and the surrounding environment, the dimension of gold elliptic cylinders is rationally adjusted to match the wavelength range suitable for luminescent circular polarizations. We start by spin-coating a PbS QDs layer on the top surface of the three types of metasurfaces on the same Si_3N_4 membrane. Thus, the amount of PbS QDs on these three types of metasurfaces is assumed to be the same. By illuminating the suspended chiral metasurface with pump light, the excitation of the hybrid emitting system leads to chirality-induced PL from the achiral QDs. The measured RCP and LCP emission intensities are shown in Figure 3b. For achiral nanoarrays, the CPL intensities of different spin states were almost the same. In contrast, it can be clearly seen that there is strong dissymmetry in the RCP and LCP emission intensities for chiral metasurfaces. The opposite CPL in enantiomers A and B serves as strong proof that the handedness of the metasurface is related to the chirality of the emission. Furthermore, another layer of PbS QDs with the same concentration was spin-coated onto the bottom surface of the metasurface. As shown in Figure 3c, we measured the RCP and LCP emission intensities for these three types of metasurfaces as well. The PL intensity is much higher with double-layer QDs since there is a linear dependence of the PL intensity with the amount of fluorophores. However, the PL intensity for the double-layer QDs is less than twice that for the single-layer case because of the lower enhancement factor of the electric fields at the bottom side. In addition, it is worth noting that the PL intensity for chiral metasurfaces with double layers of QDs demonstrated reversed polarity compared to that of chiral metasurfaces with only one layer of QDs on the top surface.

To understand the reversed polarity, we extracted CD spectra from measured transmission before and after QD coating to explore the coupling between metasurfaces and the emitted photons. The resonances of the chiral metasurfaces play a key role in the transmission and emission processes. In Figure 3d, the CD spectrum has a redshift of 55 nm when the metasurface is spin-coated with QDs on the top surface. After coating with QDs on the bottom surface, the CD spectrum manifests a redshift of 70 nm. According to our simulated spectra in Figure S8, such redshifts may be explained by the reduced refractive index difference between the QDs-metasurface and the surrounding medium.[25,39] With these red-shifts, the chirality reverses for the metasurfaces with respective enantiomers A and B at the wavelength of 1120 nm. The opposite signs of the CD at the emission wavelength from chiral metasurfaces with single and double layers of QDs might play a key role in the chirality reversal of the PL. Moreover, as shown in Figure S9, we characterized the PL properties of QDs on the same Si_3N_4 membrane outside the metasurface areas for comparison of the PL enhancement imposed by the bilayer metasurfaces. The same transmission under different circularly polarized light and equal PL properties confirms that there is no chiroptical response detected from the QDs on the Si_3N_4 membrane and further proves that the light-matter interaction between the QDs and chiral plasmons enables the manipu-

https://doi.org/10.1021/acsnano.4c05719
ACS Nano 2024, 18, 20556−20566

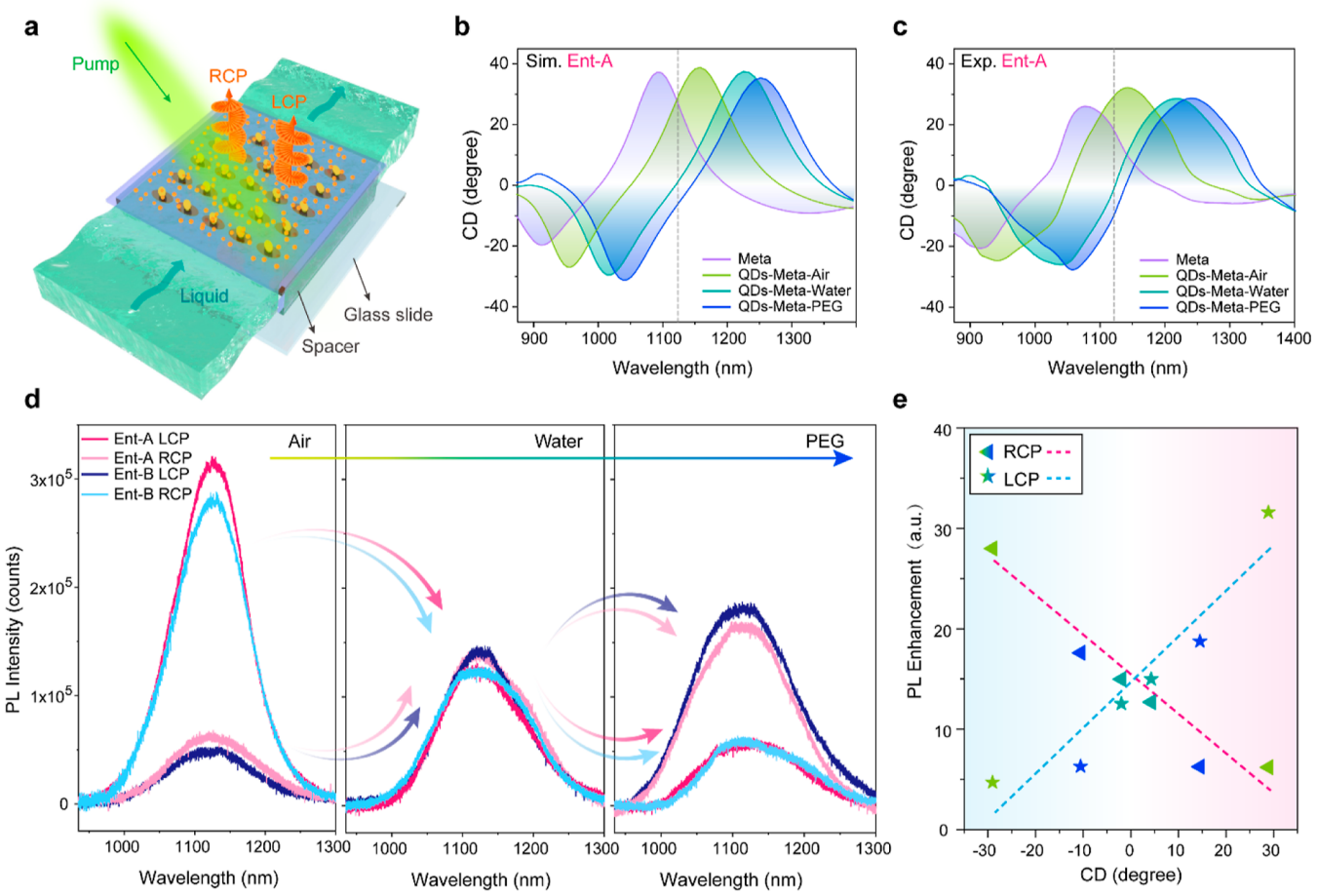

Figure 4. Switchable chiral emission with different surrounding mediums on the bottom surface. (a) Schematic diagram of PL investigation from QDs−metasurface−liquid composites. (b,c) Simulated (b) and measured (c) CD spectra of the hybrid system for enantiomer A, respectively. (d) RCP and LCP emissions from the hybrid systems with a single QD layer on the top surface and air, water, and PEG on the bottom surface, respectively. (e) PL enhancements of the RCP and LCP emission on enantiomer A and enantiomer B as a function of CD values at the wavelength of the emission peak. The dashed lines are the linear fittings. The green, cyan, and blue colors indicate the air, water, and PEG, respectively.

lation of the polarization state of CPL, which is also consistent with previous reports.[24,28,31] Compared with the PL intensities from the QDs-Si_3N_4 membrane, the LCP and RCP PL for the enantiomer A with the single layer of QDs on the top surface show enhancement factors of 29.5 and 3.8 at 1120 nm, respectively. Meanwhile, the calculated enhancement factors of RCP and LCP emission are 13.9 and 3.5 for QDs-metasurface-QDs composites. The emission enhancement from the QDs-coated metasurfaces can be attributed to the field enhancements. Although the QDs-metasurface-QDs composites have higher PL intensities, the emission enhancements decrease due to the relatively weak field enhancements at the bottom surface.

We also measured the chiral PL intensities of a single layer of QDs on the bottom surface in Figure S10. The results show that the chiral emission corresponds to the discrepancy in field enhancements induced by chiral resonances. We calculated the g_{lum} factor to assess the asymmetry of chiral emission from the hybrid emitter-metasurface systems. The g_{lum} factor is quantified as the relative difference between the RCP and LCP emission intensities

$$g_{lum} = 2 \times \frac{I_{LCP} - I_{RCP}}{I_{LCP} + I_{RCP}} \quad (3)$$

where I_{RCP} and I_{LCP} are the intensities of the RCP and LCP emissions, respectively. According to Figure 3, enantiomers A and B exhibit opposite g_{lum}. A near negligible emission difference is observed for the achiral system. Furthermore, the asymmetry in emission can be tuned by the coverage of the QDs on the bottom surface. As shown in Figure S11, a significant g_{lum} of up to 1.54 is achieved for the enantiomer A with a single layer of QDs, while a lower but flipped polarity of −1.24 is observed on the enantiomer A with the double layers of QDs. For enantiomer B, the g_{lum} is −1.47 with the single layer of QDs, and it reaches 1.34 with double layers of QDs. There is a strong correlation between the asymmetry in both transmission and emission, providing great potential for g_{lum} control imposed by the chiral metasurface with tunable CD altered via refractive index contrast.

Switchable Circularly Polarized Luminescence. To further investigate the switchable chiral emission, we change the medium surrounding the bottom surface of the metasurface with different refractive indices instead of the PbS QDs layer. As illustrated in Figure 4a, after spin-coating PbS QDs on the top surface of the metasurface, the bottom surface of the metasurface is dropped with different liquids, such as water and polyethylene glycol (PEG), and sealed by another piece of glass slide. Based on simulations in Figure S12, the handedness

https://doi.org/10.1021/acsnano.4c05719
ACS Nano 2024, 18, 20556−20566

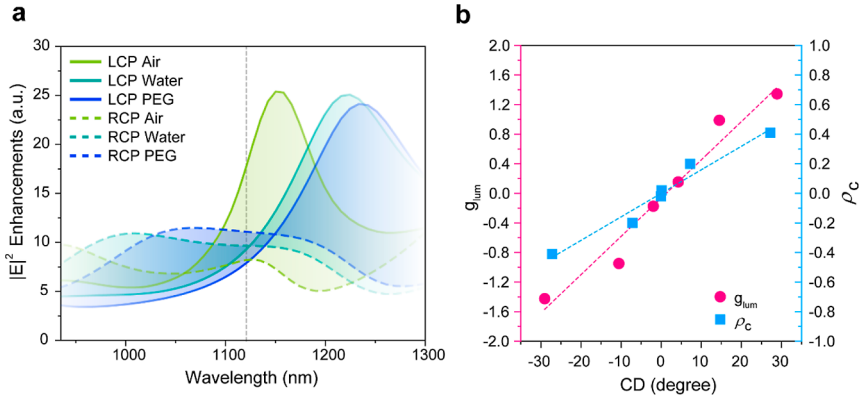

Figure 5. Correlation between g_{lum} of emission and asymmetry in local field enhancements. (a) Simulated local electric field enhancements based on reciprocity with different surrounding mediums of air, water, and PEG. (b) Measured g_{lum} and correspondingly simulated ρ_c of hybrid systems with active mediums as a function of CD values at the wavelength of the emission peak. The magenta and blue dashed lines are fitted to g_{lum} and ρ_c, respectively.

of the metasurfaces at the specific wavelength could be switched by the refractive index of the surrounding medium. By increasing the refractive index of the bottom surrounding medium, the CD spectra manifest redshifts for enantiomers A and B. The dimension of gold elliptic cylinders is adjusted slightly, and the CD value of the QDs−metasurface−water composite is designed to be 0 at the wavelength of the emission peak. Meanwhile, the CD values of QDs−metasurface−air and QDs−metasurface−PEG composites have inverse signs. In Figure 4b,c, the experimentally measured CD spectra matched well with the simulated data. We calculate the distributions of electric field enhancements for enantiomer A with the changes in the refractive index as well. As shown in Figure S13, for the QDs-metasurface-water composite, the electric field enhancements have similar distributions with slightly different maximum values under RCP and LCP light, accounting for the subequal RCP and LCP transmission.

It is clearly seen in Figure 4d that the PL intensity shows strong dissymmetry in circular polarization for the QDs-metasurface-air composite due to the significant CD of the composite. As expected, the PL intensity is similar to that in Figure 3b, claiming the robustness of the chiral emission in our optical setup. There is almost no dissymmetry in RCP and LCP emission when the bottom medium is water, mainly attributed to the achiral property at 1120 nm. With a higher refractive index, a reversed polarity is achieved with PEG compared to the one observed in QDs−metasurface−air composite. Besides the polarity of the emission, the chiral resonances of the hybrid system also determined the enhancement of the PL intensity. We calculated the PL enhancements of these three hybrid systems, as shown in Figure 4e, which provides a better understanding of the correlation between the chirality of the system and the chiral PL emission. It demonstrates that the asymmetry emission has a dependence on the CD values for both enantiomers A and B. The switchable surrounding medium on the bottom surface of the metasurface serves as a controller of the chirality of the hybrid system, ultimately modulating the circular polarization of the quantum emission.

To simulate PL enhancement and derive the Purcell factor, emitters are conventionally considered to be isotropic and are randomly distributed electric dipoles with random orientations. In our hybrid emitting system consisting of chiral plasmonic metasurfaces and QDs, the situation could be much more complicated by considering the asymmetric local photon density and emission polarization. In addition, it needs enormous computational resources to analyze all the dipoles in practice. Recently, researchers have applied the reciprocity principle to transform a light out-coupling problem to an in-coupling problem in hybrid emitting systems. As a result, the far-field emission intensity of different circularly polarized states can be simulated based on the reciprocity principle in the chiral metasurface-emitter systems to elucidate the coupling between emitters and chiral metasurfaces behind PL enhancement.[49,50] We followed reciprocity calculations to reveal the mechanism of the switchable chiral emission. For any two separable current distributions $\boldsymbol{j}_1$ and $\boldsymbol{j}_2$ in a system

$$\int \boldsymbol{j}_1 \boldsymbol{E}_2 \mathrm{d}V = \int \boldsymbol{j}_2 \boldsymbol{E}_1 \mathrm{d}V \tag{4}$$

where $\boldsymbol{E}_1$ and $\boldsymbol{E}_2$ are induced electric fields of $\boldsymbol{j}_1$ and $\boldsymbol{j}_2$, respectively. A classical dipole $\boldsymbol{p}$ represents the quantum emitter located at $\boldsymbol{r}_0$. The power of $\boldsymbol{p}$ can be expressed as

$$P = \omega \mathrm{Im}[\boldsymbol{p}^* \times \boldsymbol{E}(\boldsymbol{r}_0)]/2 \tag{5}$$

Since the current density $\boldsymbol{j}$ can be written as $\boldsymbol{j}(\boldsymbol{r}) = -i\omega\boldsymbol{p}\delta(\boldsymbol{r} - \boldsymbol{r}_0)$, where δ means the Dirac delta function, eq 4 can be then simplified to

$$\boldsymbol{p}_1 \boldsymbol{E}_2 = \boldsymbol{p}_2 \boldsymbol{E}_1 \tag{6}$$

In the hybrid emitter-metasurface system, the electric field $\boldsymbol{E}_1$ of the far-field emission by the QDs dipole $\boldsymbol{p}_1$ coupled with the metasurface can be predicted by calculating the resulting local electric field $\boldsymbol{E}_2$ excited by the dipole source $\boldsymbol{p}_2$ with the corresponding polarization at $\boldsymbol{r}_2$. The Purcell factor can be calculated and predicted according to eq 6 based on the reciprocity principle. According to eqs 5 and 6, the emission intensity by the particle at $\boldsymbol{r}_1$ in the direction $\boldsymbol{k}$ is[51]

$$I(\boldsymbol{k}, \boldsymbol{r}_1) = \frac{1}{8\pi}\sqrt{\frac{\varepsilon_0\varepsilon_2}{\mu_0}}\int_0^{2\pi}\int_0^{\pi}\left[\sum_{\mathrm{TE,TM}} |\boldsymbol{p}_1 \boldsymbol{E}_2(\boldsymbol{r}_1)|^2\right] \sin(\theta)\mathrm{d}(\theta)\mathrm{d}(\varphi) \tag{7}$$

where ε_0 and μ_0 are the permittivity and permeability in vacuum, respectively, and ε_2 is the relative permittivity at $\boldsymbol{r}_2$. TE and TM denote the TE and TM polarizations, θ is the elevation angle, and φ is the azimuthal angle. If the point dipole emitter $\boldsymbol{p}_1$ has an isotropic emission process, the

https://doi.org/10.1021/acsnano.4c05719
ACS Nano 2024, 18, 20556−20566

resulting intensity over the dipole at position r_1 is proportional to $|E_2|^2$. We achieve the degree of circular polarization of chiral emission by considering the asymmetry of field enhancements excited by different beam polarizations as[52]

$$\rho_c = \frac{\overline{|E_2^{LCP}(r)|^2} - \overline{|E_2^{RCP}(r)|^2}}{\overline{|E_2^{LCP}(r)|^2} + \overline{|E_2^{RCP}(r)|^2}} \quad (8)$$

We evaluated the integrated local electric field enhancements in the QDs region covering the metasurface of enantiomer A, as shown in Figure 5a. The field enhancement trends with various mediums closely match those observed in PL enhancements. Note that the values of simulated enhancements are slightly lower than the experimental results since, in the simulations, we only consider the field of the covering surfaces and ignore the field near the gold resonators with QDs piled. In addition, the enhanced LCP PL peak redshifts with an increase in the refractive index. Figure 5b shows the measured g_{lum} and the calculated ρ_c according to eq 8. Overall, both g_{lum} and ρ_c are proportional to the CD in the hybrid emitting system. The changes in g_{lum} and ρ_c illustrate a similar trend, which is consistent with the reciprocity principle. When the surrounding medium is changed from air to PEG, the g_{lum} emission at 1120 nm reverses from −1.42 to 0.98, with a significant difference of 2.4. The reversible g_{lum} of chiral emission as a function of CD values is a predominant serviceable feature of the suspended twisted stacking metasurface.

CONCLUSIONS

In summary, a chiral plasmonic metasurface consisting of twisted stacking gold nanoarrays spaced by an ultrathin Si_3N_4 membrane has been realized via a single-step EBL exposure. We demonstrated a significant chiroptical response of the twisted stacking metasurface with an optical chirality of 309° μm^{-1}. Combining the PbS QDs with this chiral metasurface, we have proposed and performed a hybrid emitting system exhibiting strong enhancement and polarized modulation of PL emission due to the coupling between chiral plasmons and QDs. In addition, according to reciprocity, the asymmetry of the circularly polarized emission is directly correlated to the field enhancements induced by chiral resonance in the hybrid system. The chiral resonance of the QDs−metasurface−medium composite can be controlled by changing the refractive index of the surrounding medium at the bottom surface of the metasurface. The switchable chirality of the composite modulates the circular polarization of the emission with an inversely tuned g_{lum}. The maximum value of g_{lum} can reach 1.54 at the emission wavelength of 1120 nm, and the difference of tunable g_{lum} is up to 2.4.

This QDs−metasurface−medium composite performs a key demonstration of the switchable enhanced chiral fields, which can be perceptively exploited to efficiently reverse the polarization state of PL due to chiral-selective light-matter interactions for sensing applications and display technologies. While this work is focused on demonstrating the proof-of-concept of CPL reversing by changing the refractive index in the liquid environment, the use of this light-emitting metasurface is not limited to solid environments and will be further studied for all-optically integrated devices of dynamic imaging, lighting, and lasing.

MATERIALS AND METHODS

Metasurface Fabrication. As shown in Figure S1, the suspended twisted stacking metasurfaces were fabricated on a suspended Si_3N_4 membrane via a single-step EBL process. The commercially available Si_3N_4 membrane (CleanSiN, China) with a thickness of 50 nm was used as the supporting layer. After hydrophilic treatment, the top surface of the Si_3N_4 membrane was spin-coated with 230 nm AR-P 6200.09 (Allresist, Germany), and the bottom surface was spin-coated with 120 nm PMMA 3% (diluted by AR-P 672.045 950k 4.5 wt % in anisole, Allresist, Germany). The thicknesses of the resists were measured by a surface profiler (KLA-Tencor, P-7). The AR-P 6200.09 was spin-coated with a revolving speed of 5000 rpm for 60 s and baked at 150 °C for 60 s, while the PMMA was spun at 3000 rpm for 60 s and immediately baked at 180 °C for 120 s to remove the solvent. Then, a layer of water-soluble conductive polymer (AR-PC 5090.02, Allresist, Germany) was spin-coated on the top resist layer to help improve the electrical conductivity. The resists were then patterned via an EBL system (Nanobeam nB5, UK) with an acceleration voltage of 80 kV and a beam current of 2 nA. The exposure doses for AR-P 6200.09 and PMMA were 250 and 900 $\mu C\ cm^{-2}$, respectively. The designed patterns were exposed to both top and bottom resists simultaneously in a single-step EBL process. The conductive layer was then removed with deionized water. The pattern development for AR-P 6200.09 and PMMA was done in AR 600−546 (Allresist, Germany) for 60 and 80 s, respectively. Then, a 1.5 nm Ti adhesion layer and a 25 nm gold layer were deposited on both surfaces via an electron-beam evaporator (HHV TF500, UK). At the end, a lift-off process was carried out in the remover AR 600−71 (Allresist, Germany), and the suspended twisted stacking metasurfaces were finally achieved.

QDs Coating. The PbS QDs (Mesolight, China) were dissolved in chlorobenzene and formed a solution with a concentration of 10 mg mL^{-1}. Subsequently, a volume of 10 μL of PbS QDs solution was spin-coated at 2000 rpm on the surface of the suspended chiral metasurfaces, which had been cleaned by ultraviolet ozone in advance. After baking at 50 °C for 5 min, the solvent evaporated. The PbS QDs layer on the bottom surface was coated at the same conditions with 5 μL of PbS QDs solution. Then, the QDs−metasurface−QDs composite was prepared for experimental investigation. For switching the chirality of the metasurface, after spin-coating PbS QDs on the top surface of the suspended bilayer metasurface, the bottom surface of the metasurface was dropped with 5 μL of water or PEG and then placed on a glass slide to form a fluidic cell.

Structural Characterization. Morphologies of the fabricated suspended bilayer metasurfaces and the QDs−metasurface−QDs composite were characterized using field emission scanning electron microscopy (FESEM, Merlin, Zeiss) at a 2 kV acceleration voltage. Energy dispersive spectroscopy (EDS) analysis was carried out with the same microscope to confirm the elemental composition and distribution of the QDs-metasurface-QD composite. For the EDS analysis, the acceleration voltage was set to 10 kV.

Optical Characterization. The optical transmission spectra were measured via a microspectrophotometer system (CRAIC 20/30PV). The schematic of the optical setup is shown in Figure S14a. A broadband light source (70 W xenon lamp, Olympus) sequentially passed through a linear polarizer (Thorlabs, WP25M-UB, 250−4000 nm) and a quarter-wave plate (QWP, Thorlabs, SAQWP05M-1700, 600−2700 nm). Circularly polarized light was generated with angles of ±45° between the optical axis of the linear polarizer and the fast axis of the QWP. A 100× objective lens (NA = 0.8) was used to collect transmitted light. Then, the light was guided to the camera and spectrometer by a beam splitter. An aperture set was placed before the spectrometer, which was used to confine the testing area of the sample under the tests. In our experiments, a testing area of 5 × 5 μm^2 was selected. An imaging camera helped us perform in situ measurements. For PL characterization, the PL spectra of the PbS QDs were measured by a microspectral system constituted with a semiconductor continuous laser (Changchun New Industries Optoelectronics Technology, 532 nm), an optical microscope (Olympus, BX53),

https://doi.org/10.1021/acsnano.4c05719
ACS Nano 2024, 18, 20556−20566

and a near-infrared spectrograph (Princeton, NIRvana). Figure S14b shows the schematic corresponding optical setup. The excitation laser beam was fixed with a power of 0.1 mW and focused on the samples from the bottom with the spot size of 20 μm. The numerical aperture of the objective lens (Olympus, 100×) was 0.8. All PL spectra were collected with the same integration time of 10 s. The measured sample area was limited to 5 μm × 5 μm using a variable aperture, containing approximately 100 meta-atoms, which can be completely covered by the focused excitation laser spot for uniform pumping. The excited PL was analyzed through an achromatic QWP (Thorlabs, SAQWP05M-1700, 600−2700 nm) and a linear polarizer (Thorlabs, WP25M-UB, 250−4000 nm) with a proper configuration. A 550 nm long-pass filter (Thorlabs, FELH0550) was used to block the pumping laser. The absorbance of PbS QDs solution (10 mg mL^{-1} in chlorobenzene) was measured by a UV−vis spectrophotometer (METASH, UV-5200PC, China). The solution was transferred to a double-pass quartz cuvette for the measurements. The background was taken from the air.

Numerical Simulation. To calculate transmission spectra, electric field distributions, and superchiral fields of the metasurfaces, the finite-difference time-domain method was used in this work. In our simulations, the refractive indices of gold and Si_3N_4 were based on the data from our previous work.[45] The refractive index of the PbS QDs layer with a thickness of 11.7 nm was confirmed by an ellipsometer (Horiba, TF-UVISEL), as shown in Figure S15. In addition, the refractive indices of air, water, and PEG were set at 1, 1.33, and 1.47, respectively. A unit of the chiral meta-atom was simulated with periodic boundary conditions along the *x*- and *y*-axes and a perfectly matched layer along the *z*-axis (the propagation direction of light waves). The incident circularly polarized light propagated along the *z*-axis, which is synthesized by two orthogonal linearly polarized plane waves with equal amplitudes (an x-polarized plane wave with 0° phase and a y-polarized plane wave with +90° or −90° phase). A uniform mesh size of 2 nm in all three dimensions was used to cover the region of structures. The time step $\Delta t = 1 \times 10^{-18}$ s satisfied the Courant stability.[53]

ASSOCIATED CONTENT

Supporting Information

The Supporting Information is available free of charge at https://pubs.acs.org/doi/10.1021/acsnano.4c05719.

Metasurface fabrication; simulated CD spectra of the twisted stacking metasurfaces with different twisted angle ϑ; transmission spectra of various incident/output handedness; comparison of the optical chirality of chiral metasurfaces with respect to their thicknesses; numerical simulations of field enhancement and superchiral fields; simulated absorption; mapping distribution and EDS characterization; measured and simulated transmission spectra of metasurfaces coupling with QDs; comparison of transmission and emission enhancement characteristics with the blank Si_3N_4 membrane; PL investigation from metasurface−QDs and QDs−metasurface−QDs; g_{lum} factors of chiral emission for the metasurfaces with the single layer and double layers of PbS QDs; tuning the chiral resonances by changing the surrounding medium; electric field distributions with changes of the refractive index; schematic diagrams of experimental setups for transmission spectra measurement and PL characterization; measured refractive index of the PbS QDs layer (PDF)

AUTHOR INFORMATION

Corresponding Authors

Tun Cao − *School of Optoelectronic Engineering and Instrumentation Science, Dalian University of Technology, Dalian 116024, China;* orcid.org/0000-0003-3536-0092; Email: caotun1806@dlut.edu.cn

Yan-Qing Lu − *College of Engineering and Applied Sciences, Nanjing University, Nanjing 210093, China;* orcid.org/0000-0001-6151-8557; Email: yqlu@nju.edu.cn

Yan Jun Liu − *Department of Electrical and Electronic Engineering, Southern University of Science and Technology, Shenzhen 518055, China; State Key Laboratory of Optical Fiber and Cable Manufacture Technology and Shenzhen Engineering Research Center for High Resolution Light Field Display and Technology, Southern University of Science and Technology, Shenzhen 518055, China;* orcid.org/0000-0001-8724-0434; Email: yjliu@sustech.edu.cn

Authors

Mengjia Cen − *Department of Electrical and Electronic Engineering, Southern University of Science and Technology, Shenzhen 518055, China; State Key Laboratory of Optical Fiber and Cable Manufacture Technology and Shenzhen Engineering Research Center for High Resolution Light Field Display and Technology, Southern University of Science and Technology, Shenzhen 518055, China; School of Optoelectronic Engineering and Instrumentation Science, Dalian University of Technology, Dalian 116024, China*

Jianxun Liu − *Department of Electrical and Electronic Engineering, Southern University of Science and Technology, Shenzhen 518055, China; State Key Laboratory of Optical Fiber and Cable Manufacture Technology and Shenzhen Engineering Research Center for High Resolution Light Field Display and Technology, Southern University of Science and Technology, Shenzhen 518055, China*

Jiawei Wang − *Department of Electrical and Electronic Engineering, Southern University of Science and Technology, Shenzhen 518055, China; State Key Laboratory of Optical Fiber and Cable Manufacture Technology and Shenzhen Engineering Research Center for High Resolution Light Field Display and Technology, Southern University of Science and Technology, Shenzhen 518055, China*

Ye Li − *Department of Electrical and Electronic Engineering, Southern University of Science and Technology, Shenzhen 518055, China; State Key Laboratory of Optical Fiber and Cable Manufacture Technology and Shenzhen Engineering Research Center for High Resolution Light Field Display and Technology, Southern University of Science and Technology, Shenzhen 518055, China*

Wenfeng Cai − *Department of Electrical and Electronic Engineering, Southern University of Science and Technology, Shenzhen 518055, China; State Key Laboratory of Optical Fiber and Cable Manufacture Technology and Shenzhen Engineering Research Center for High Resolution Light Field Display and Technology, Southern University of Science and Technology, Shenzhen 518055, China*

Ming Cheng − *Department of Electrical and Electronic Engineering, Southern University of Science and Technology, Shenzhen 518055, China; State Key Laboratory of Optical Fiber and Cable Manufacture Technology and Shenzhen Engineering Research Center for High Resolution Light Field Display and Technology, Southern University of Science and Technology, Shenzhen 518055, China*

Delai Kong − *Department of Electrical and Electronic Engineering, Southern University of Science and Technology, Shenzhen 518055, China; State Key Laboratory of Optical Fiber and Cable Manufacture Technology and Shenzhen*

Engineering Research Center for High Resolution Light Field Display and Technology, Southern University of Science and Technology, Shenzhen 518055, China

Xiaoying Tang − *Department of Electrical and Electronic Engineering, Southern University of Science and Technology, Shenzhen 518055, China; State Key Laboratory of Optical Fiber and Cable Manufacture Technology, Southern University of Science and Technology, Shenzhen 518055, China*

Complete contact information is available at: https://pubs.acs.org/10.1021/acsnano.4c05719

Author Contributions

#M.C. and J.L. contributed equally to this work. Y.J.L. conceived the project and designed the experiment. M.C., J.W., and Y.L. fabricated samples. M.C. and J.L. carried out the measurements. M.C. performed simulations and wrote the manuscript. W.C., M.C., D.K., and X.T. analyzed the data. T.C., Y.-Q.L., and Y.J.L. provided theoretical explanations and supervised the project. All authors discussed the results and contributed to the final manuscript.

Notes

The authors declare no competing financial interest.

ACKNOWLEDGMENTS

The authors acknowledge financial support by the National Key R&D Program of China (grant no. 2022YFA1203702), the National Natural Science Foundation of China (grant no. 62075093 and 62211530039), the Guangdong Innovative and Entrepreneurial Research Team Program (grant no. 2017ZT07C071), the Shenzhen Science and Technology Innovation Commission (grant no. JCYJ20220818100413030), the Shenzhen Development and Reform Commission (grant no. XMHT20220114005), and High Level of Special Funds from Southern University of Science and Technology (grant no. G030230001 and G03034K004). This study was also funded by the Key Lab of Modern Optical Technologies of the Education Ministry of China, Soochow University (grant no. KJS2132). The authors acknowledge the assistance of SUSTech Core Research Facilities.

ABBREVIATIONS

CD, circular dichroism; CPL, circularly polarized luminescence; PL, photoluminescence; QDs, quantum dots; EBL, electron beam lithography; RCP, right circularly polarized; LCP, left circularly polarized; SEM, scanning electron microscopy; PEG, polyethylene glycol; EDS, energy dispersive spectroscopy; QWP, quarter-wave plate

REFERENCES

(1) Zhang, X.; Liu, Y.; Han, J.; Kivshar, Y.; Song, Q. Chiral Emission from Resonant Metasurfaces. *Science* **2022**, *377*, 1215−1218.

(2) Lodahl, P.; Mahmoodian, S.; Stobbe, S.; Rauschenbeutel, A.; Schneeweiss, P.; Volz, J.; Pichler, H.; Zoller, P. Chiral Quantum Optics. *Nature* **2017**, *541*, 473−480.

(3) Kim, Y. H.; Zhai, Y.; Lu, H.; Pan, X.; Xiao, C.; Gaulding, E. A.; Harvey, S. P.; Berry, J. J.; Vardeny, Z. V.; Luther, J. M.; Beard, M. C. Chiral-Induced Spin Selectivity Enables a Room-Temperature Spin Light-Emitting Diode. *Science* **2021**, *371*, 1129−1133.

(4) MacKenzie, L. E.; Pal, R. Circularly Polarized Lanthanide Luminescence for Advanced Security Inks. *Nat. Rev. Chem* **2020**, *5* (2), 109−124.

(5) Xu, M.; Ma, C.; Zhou, J.; Liu, Y.; Wu, X.; Luo, S.; Li, W.; Yu, H.; Wang, Y.; Chen, Z.; Li, J.; Liu, S. Assembling Semiconductor Quantum Dots in Hierarchical Photonic Cellulose Nanocrystal Films: Circularly Polarized Luminescent Nanomaterials as Optical Coding Labels. *J. Mater. Chem. C* **2019**, *7* (44), 13794−13802.

(6) Nistanaki, S. K.; Williams, C. G.; Wigman, B.; Wong, J. J.; Haas, B. C.; Popov, S.; Werth, J.; Sigman, M. S.; Houk, K. N.; Nelson, H. M. Catalytic Asymmetric C-H Insertion Reactions of Vinyl Carbocations. *Science* **2022**, *378*, 1085−1091.

(7) Hao, C.; Xu, L.; Kuang, H.; Xu, C. Artificial Chiral Probes and Bioapplications. *Adv. Mater.* **2020**, *32* (41), 1802075.

(8) Zhao, Y.; Askarpour, A. N.; Sun, L.; Shi, J.; Li, X.; Alù, A. Chirality Detection of Enantiomers Using Twisted Optical Metamaterials. *Nat. Commun.* **2017**, *8*, 14180.

(9) Zhan, X.; Xu, F. F.; Zhou, Z.; Yan, Y.; Yao, J.; Zhao, Y. S. 3D Laser Displays Based on Circularly Polarized Lasing from Cholesteric Liquid Crystal Arrays. *Adv. Mater.* **2021**, *33* (37), 2104418.

(10) Han, D.; Li, C.; Jiang, C.; Jin, X.; Wang, X.; Chen, R.; Cheng, J.; Duan, P. Endowing Inorganic Nanomaterials with Circularly Polarized Luminescence. *Aggregate* **2022**, *3*, No. e148.

(11) Sang, Y.; Han, J.; Zhao, T.; Duan, P.; Liu, M. Circularly Polarized Luminescence in Nanoassemblies: Generation, Amplification, and Application. *Adv. Mater.* **2020**, *32* (41), 1900110.

(12) Yang, D.; Duan, P.; Liu, M. Dual Upconverted and Downconverted Circularly Polarized Luminescence in Donor-Acceptor Assemblies. *Angew. Chem.* **2018**, *130* (30), 9501−9505.

(13) Deng, Y.; Wang, M.; Zhuang, Y.; Liu, S.; Huang, W.; Zhao, Q. Circularly Polarized Luminescence from Organic Micro-/Nano-Structures. *Light Sci. Appl.* **2021**, *10*, 76.

(14) Mayorga Burrezo, P.; Jiménez, V. G.; Blasi, D.; Ratera, I.; Campaña, A. G.; Veciana, J. Organic Free Radicals as Circularly Polarized Luminescence Emitters. *Angew. Chem., Int. Ed.* **2019**, *58* (45), 16282−16288.

(15) Cheng, Q.; Hao, A.; Xing, P. A Chemosensor-Based Chiral Coassembly with Switchable Circularly Polarized Luminescence. *Nat. Commun.* **2021**, *12*, 6320.

(16) Yang, Z.; Wei, Y.; Wei, J.; Yang, Z. Chiral Superstructures of Inorganic Nanorods by Macroscopic Mechanical Grinding. *Nat. Commun.* **2022**, *13*, 5844.

(17) Gao, P.; Zhang, K.; Ren, D.; Liu, H.; Zhang, H.; Fu, H.; Ma, L.; Li, D. Host-Guest Chemistry of Chiral MOFs for Multicolor Circularly Polarized Luminescence Including Room Temperature Phosphorescence. *Adv. Funct. Mater.* **2023**, *33* (26), 202300105.

(18) Chen, L.; Hao, C.; Cai, J.; Chen, C.; Ma, W.; Xu, C.; Xu, L.; Kuang, H. Chiral Self-Assembled Film from Semiconductor Nanorods with Ultra-Strong Circularly Polarized Luminescence. *Angew. Chem., Int. Ed.* **2021**, *60* (50), 26276−26280.

(19) Yang, X.; Lv, J.; Zhang, J.; Shen, T.; Xing, T.; Qi, F.; Ma, S.; Gao, X.; Zhang, W.; Tang, Z. Tunable Circularly Polarized Luminescence from Inorganic Chiral Photonic Crystals Doped with Quantum Dots. *Angew. Chem., Int. Ed.* **2022**, *61* (29), No. e202201674.

(20) Valev, V. K.; Baumberg, J. J.; Sibilia, C.; Verbiest, T. Chirality and Chiroptical Effects in Plasmonic Nanostructures: Fundamentals, Recent Progress, and Outlook. *Adv. Mater.* **2013**, *25* (18), 2517−2534.

(21) Tang, Y.; Cohen, A. E. Optical Chirality and Its Interaction with Matter. *Phys. Rev. Lett.* **2010**, *104* (16), 163901.

(22) Hentschel, M.; Schäferling, M.; Duan, X.; Giessen, H.; Liu, N. Chiral Plasmonics. *Sci. Adv.* **2017**, *3* (5), No. e1602735.

(23) Yu, N.; Capasso, F. Flat Optics with Designer Metasurfaces. *Nat. Mater.* **2014**, *13* (2), 139−150.

(24) Cotrufo, M.; Osorio, C. I.; Koenderink, A. F. Spin-Dependent Emission from Arrays of Planar Chiral Nanoantennas Due to Lattice and Localized Plasmon Resonances. *ACS Nano* **2016**, *10* (3), 3389−3397.

(25) Yang, A.; Hoang, T. B.; Dridi, M.; Deeb, C.; Mikkelsen, M. H.; Schatz, G. C.; Odom, T. W. Real-Time Tunable Lasing from Plasmonic Nanocavity Arrays. *Nat. Commun.* **2015**, *6*, 6939.

(26) Vinçon, I.; Wendisch, F. J.; De Gregorio, D.; Pritzl, S. D.; Akkerman, Q. A.; Ren, H.; De S. Menezes, L.; Maier, S. A.; Feldmann, J. Strong Polarization Dependent Nonlinear Excitation of a Perovskite Nanocrystal Monolayer on a Chiral Dielectric Nanoantenna Array. *ACS Photonics* **2022**, *9*, 3506−3514.
(27) Lim, Y.; Seo, I. C.; An, S. C.; Kim, Y.; Park, C.; Woo, B. H.; Kim, S.; Park, H. R.; Jun, Y. C. Maximally Chiral Emission via Chiral Quasibound States in the Continuum. *Laser Photon. Rev.* **2022**, *17*, 2200611.
(28) He, H.; Cen, M.; Wang, J.; Xu, Y.; Liu, J.; Cai, W.; Kong, D.; Li, K.; Luo, D.; Cao, T.; Liu, Y. J. Plasmonic Chiral Metasurface-Induced Upconverted Circularly Polarized Luminescence from Achiral Upconversion Nanoparticles. *ACS Appl. Mater. Interfaces* **2022**, *14*, 53981−53989.
(29) Pachidis, P.; Cote, B. M.; Ferry, V. E. Tuning the Polarization and Directionality of Photoluminescence of Achiral Quantum Dot Films with Chiral Nanorod Dimer Arrays: Implications for Luminescent Applications. *ACS Appl. Nano Mater.* **2019**, *2* (9), 5681−5687.
(30) Rodrigues, S. P.; Cui, Y.; Lan, S.; Kang, L.; Cai, W. Metamaterials Enable Chiral-Selective Enhancement of Two-Photon Luminescence from Quantum Emitters. *Adv. Mater.* **2015**, *27* (6), 1124−1130.
(31) Wang, Z.; Wang, Y.; Adamo, G.; Teng, J.; Sun, H. Induced Optical Chirality and Circularly Polarized Emission from Achiral CdSe/ZnS Quantum Dots via Resonantly Coupling with Plasmonic Chiral Metasurfaces. *Laser Photon. Rev.* **2019**, *13* (3), 1800276.
(32) Wang, Z.; Zhang, H.; Hao, A.; Zhao, Y.; Xing, P. Modular Molecular Self-Assembly for Diversified Chiroptical Systems. *Small* **2020**, *16* (30), 2002036.
(33) Neubrech, F.; Hentschel, M.; Liu, N. Reconfigurable Plasmonic Chirality: Fundamentals and Applications. *Adv. Mater.* **2020**, *32* (41), 1905640.
(34) Xiao, D.; Liu, Y. J.; Yin, S.; Liu, J.; Ji, W.; Wang, B.; Luo, D.; Li, G.; Sun, X. W. Liquid-Crystal-Loaded Chiral Metasurfaces for Reconfigurable Multiband Spin-Selective Light Absorption. *Opt. Express* **2018**, *26* (19), 25305−25314.
(35) Liu, J.; Zeng, H.; Cheng, M.; Wang, Z.; Wang, J.; Cen, M.; Luo, D.; Priimagi, A.; Liu, Y. J. Photoelastic Plasmonic Metasurfaces with Ultra-Large Near Infrared Spectral Tuning. *Mater. Horiz.* **2022**, *9* (3), 942−951.
(36) Liu, Z.; Xu, Y.; Ji, C. Y.; Chen, S.; Li, X.; Zhang, X.; Yao, Y.; Li, J. Fano-Enhanced Circular Dichroism in Deformable Stereo Metasurfaces. *Adv. Mater.* **2020**, *32* (8), 1907077.
(37) Jun, Y. C.; Huang, K. C. Y.; Brongersma, M. L. Plasmonic Beaming and Active Control over Fluorescent Emission. *Nat. Commun.* **2011**, *2*, 283.
(38) Bohn, J.; Bucher, T.; Chong, K. E.; Komar, A.; Choi, D. Y.; Neshev, D. N.; Kivshar, Y. S.; Pertsch, T.; Staude, I. Active Tuning of Spontaneous Emission by Mie-Resonant Dielectric Metasurfaces. *Nano Lett.* **2018**, *18* (6), 3461−3465.
(39) Abass, A.; Rodriguez, S. R. K.; Ako, T.; Aubert, T.; Verschuuren, M.; Van Thourhout, D.; Beeckman, J.; Hens, Z.; Gómez Rivas, J.; Maes, B. Active Liquid Crystal Tuning of Metallic Nanoantenna Enhanced Light Emission from Colloidal Quantum Dots. *Nano Lett.* **2014**, *14* (10), 5555−5560.
(40) Dai, C.; Wan, S.; Li, Z.; Shi, Y.; Zhang, S.; Li, Z. Switchable Unidirectional Emissions from Hydrogel Gratings with Integrated Carbon Quantum Dots. *Nat. Commun.* **2024**, *15*, 845.
(41) Zhang, S.; Zhou, J.; Park, Y. S.; Rho, J.; Singh, R.; Nam, S.; Azad, A. K.; Chen, H. T.; Yin, X.; Taylor, A. J.; Zhang, X. Photoinduced Handedness Switching in Terahertz Chiral Metamolecules. *Nat. Commun.* **2012**, *3*, 942.
(42) Cong, L.; Pitchappa, P.; Wang, N.; Singh, R. Electrically Programmable Terahertz Diatomic Metamolecules for Chiral Optical Control. *Research* **2019**, *2019*, 7084251.
(43) Wu, Z.; Chen, X.; Wang, M.; Dong, J.; Zheng, Y. High-Performance Ultrathin Active Chiral Metamaterials. *ACS Nano* **2018**, *12* (5), 5030−5041.
(44) Han, Z.; Wang, F.; Sun, J.; Wang, X.; Tang, Z. Ultrathin Twisted Stacked Gap-Plasmon Metasurface with Giant and Tunable Shortwave Infrared Chirality. *Adv. Opt. Mater.* **2023**, *11* (23), 202301022.
(45) Cen, M.; Wang, J.; Liu, J.; He, H.; Li, K.; Cai, W.; Cao, T.; Liu, Y. J. Ultrathin Suspended Chiral Metasurfaces for Enantiodiscrimination. *Adv. Mater.* **2022**, *34*, 2203956.
(46) Probst, P. T.; Mayer, M.; Gupta, V.; Steiner, A. M.; Zhou, Z.; Auernhammer, G. K.; König, T. A. F.; Fery, A. Mechano-Tunable Chiral Metasurfaces via Colloidal Assembly. *Nat. Mater.* **2021**, *20* (7), 1024−1028.
(47) Mun, J.; Kim, M.; Yang, Y.; Badloe, T.; Ni, J.; Chen, Y.; Qiu, C. W.; Rho, J. Electromagnetic Chirality: From Fundamentals to Nontraditional Chiroptical Phenomena. *Light Sci. Appl.* **2020**, *9* (1), 139.
(48) Hendry, E.; Carpy, T.; Johnston, J.; Popland, M.; Mikhaylovskiy, R. V.; Lapthorn, A. J.; Kelly, S. M.; Barron, L. D.; Gadegaard, N.; Kadodwala, M. Ultrasensitive Detection and Characterization of Biomolecules Using Superchiral Fields. *Nat. Nanotechnol.* **2010**, *5* (11), 783−787.
(49) Zhang, S.; Martins, E. R.; Diyaf, A. G.; Wilson, J. I. B.; Turnbull, G. A.; Samuel, I. D. W. Calculation of the Emission Power Distribution of Microstructured OLEDs Using the Reciprocity Theorem. *Synth. Met.* **2015**, *205*, 127−133.
(50) Zhang, Z.; Xu, C.; Liu, C.; Lang, M.; Zhang, Y.; Li, M.; Lu, W.; Chen, Z.; Wang, C.; Wang, S.; Li, X. Dual Control of Enhanced Quasi-Bound States in the Continuum Emission from Resonant C-Si Metasurfaces. *Nano Lett.* **2023**, *23* (16), 7584−7592.
(51) Vaskin, A.; Kolkowski, R.; Koenderink, A. F.; Staude, I. Light-Emitting Metasurfaces. *Nanophotonics* **2019**, *8* (7), 1151−1198.
(52) Maksimov, A. A.; Tartakovskii, I. I.; Filatov, E. V.; Lobanov, S. V.; Gippius, N. A.; Tikhodeev, S. G.; Schneider, C.; Kamp, M.; Maier, S.; Höfling, S.; Kulakovskii, V. D. Circularly Polarized Light Emission from Chiral Spatially-Structured Planar Semiconductor Microcavities. *Phys. Rev. B* **2014**, *89* (4), 045316.
(53) Zheng, F.; Chen, Z.; Zhang, J. A Finite-Difference Time-Domain Method without the Courant Stability Conditions. *IEEE Microw. Guid. Wave Lett.* **1999**, *9* (11), 441−443.

https://doi.org/10.1021/acsnano.4c05719
ACS Nano 2024, 18, 20556−20566